

Modified and controllable dispersion interaction in a 1D waveguide geometry

Harald R. Haakh^{1,*} and Stefan Scheel^{2,†}

¹Max Planck Institute for the Science of Light, Günther-Scharowsky-Straße 1/24, D-91058 Erlangen, Germany.

²Institut für Physik, Universität Rostock, Universitätsplatz 3, D-18055 Rostock, Germany

(Dated: April 2, 2015)

Dispersion interactions such as the van der Waals interaction between atoms or molecules derive from quantum fluctuations of the electromagnetic field and can be understood as the exchange of virtual photons between the interacting partners. Any modification of the environment in which those photons propagate will thus invariably lead to an alteration of the van der Waals interaction. Here we show how the two-body dispersion interaction inside a cylindrical waveguide can be made to decay asymptotically exponentially, and how this effect sensitively depends on the material properties and the length scales of the problem, eventually leading to the possibility of controllable interactions. Further, we discuss the possibility to detect the retarded van der Waals interaction by resonant enhancement of the interaction between Rydberg atoms in the light of long-range potentials due to guided modes.

PACS numbers: 34.20.Cf, 34.35.+a, 42.50.Ct, 42.82.Et

I. INTRODUCTION

Dispersion interactions such as the van der Waals (vdW) interaction are best known for generating attractive potentials between electrically or magnetically neutral yet polarizable quantum emitters as a direct consequence of the quantized nature of the electromagnetic field. While seminal work studied either such interactions between two quantum emitters embedded in a bulk medium [1–4] or the (Casimir–Polder) dispersion interaction of a single quantum emitter with a macroscopic body [2, 4], a question of interest is how two-body dispersion potentials can be modified by the presence of macroscopic external boundaries that affect the mode structure of the electromagnetic fields and, hence, also the vacuum fluctuations [5–9]. Very strong effects can be expected in waveguides where well-defined modes induce long-range correlations. For a single emitter in a cylindrical waveguide near a cavity resonance, Ref. [10] predicted strong enhancement of the single-particle–wall interaction at certain resonant radii. Recently, the two-body dispersion interaction in an idealized metallic rectangular waveguide was shown to decay asymptotically exponentially with distance [11] if a lower mode cut-off is present, whereas the fundamental mode of a transmission line provides a significant enhancement of the dispersion potential [12].

Here, we consider the case of hollow cylindrical tubes (capillaries) of a metallic or semiconducting material, or dielectric cylinder waveguides (optical fibers) that contain a pair of quantum emitters, as depicted in Fig. 1, and apply the approach of macroscopic QED to gain a deeper understanding of the underlying mechanisms and study the impact of material properties beyond the ap-

proximation of ideal conductors. We present numerical results that agree well with analytic calculations. Our results show how a modification of the boundary conditions imposed by a realistic material can be used to modify the van der Waals potential significantly. The drastic difference between dielectric and metallic boundary conditions make the use of phase-change materials particularly interesting.

We further discuss the role of resonant potential contributions which arise from the emission of real photons by initially excited atoms. In a waveguide environment, these may bring a discussion of the still elusive far-field potential into reach. Owing to the rapid decrease of the vdW interaction with the emitter separation, detection of the retarded potential is generally exceedingly difficult. A possible alternative to use highly excited Rydberg states with their vastly enhanced vdW interaction [13, 14] will be discussed. A detailed review of the dyadic Green function in a waveguide environment is given in the Appendix.

II. WAVEGUIDE-ASSISTED DISPERSION POTENTIAL

A. General approach

The vdW dispersion potential is obtained from the mutually induced dipole-dipole interaction within fourth-order perturbation theory. We obtain the general expressions within the framework of macroscopic QED [4, 15, 16], where the mode structure of an arbitrary dispersive and dissipative environment is encoded in the classical dyadic Green function $\mathcal{G}(\mathbf{r}, \mathbf{r}', \omega)$.

Evaluating the dispersion potential near an interface, one finds single-body energy shifts which depend only on the position of a single emitter [6, 7]. Here, we focus on the irreducible two-body contribution that depends on the positions of both emitters. This dispersion potential

*Electronic address: harald.haakh@mpl.mpg.de

†Electronic address: stefan.scheel@uni-rostock.de

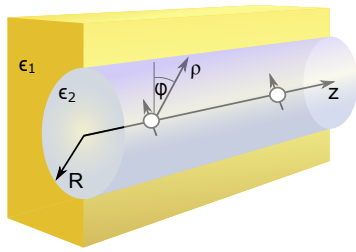


FIG. 1: Sketch of the system: two emitters are placed on the axis of a cylindrical waveguide of radius R , separated by a distance z . The core medium ϵ_2 is embedded in a low-index (or metallic) medium ϵ_1 to form a dielectric (or conducting) waveguide.

is given by the well-known expression [4, 7, 16, 17]

$$U = -\text{Im } \hbar \int_0^\infty \frac{d\omega}{2\pi} \frac{\omega^4}{c^4 \epsilon_0^2} \times \times \text{Tr} \left[\boldsymbol{\alpha}^{(1)}(\omega) \cdot \mathcal{G}(\mathbf{r}_1, \mathbf{r}_2, \omega) \cdot \boldsymbol{\alpha}^{(2)}(\omega) \cdot \mathcal{G}(\mathbf{r}_2, \mathbf{r}_1, \omega) \right]. \quad (1)$$

For two-level emitters with resonance frequencies Ω_n and transition dipole moments $\mathbf{d}^{(n)}$ in the ground state, we have the polarizability tensor

$$\boldsymbol{\alpha}^{(n)} = \frac{2\mathbf{d}^{(n)} \otimes \mathbf{d}^{(n)*} \Omega_n / \hbar}{\Omega_n^2 - (\omega + i0^+)^2}. \quad (2)$$

We consider two identical particles with a preferred polarization axis. Denoting by α and \mathcal{G} the projections of the polarizability and the Green tensor onto this direction, we obtain scalar expressions that can be expressed at imaginary frequencies as

$$U = -\hbar \int_0^\infty \frac{d\xi}{2\pi} \frac{\xi^4}{c^4 \epsilon_0^2} \alpha^2(i\xi) \mathcal{G}^2(\mathbf{r}_1, \mathbf{r}_2, i\xi). \quad (3)$$

We now turn to the setup sketched in Fig. 1, where two identical particles with either purely axial or radial polarizability are placed on the axis of a cylinder of radius R and separated by a distance z . In the presence of boundaries, the scattering ansatz is employed $\mathcal{G} = \mathcal{G}^{(0)} + \mathcal{G}^{(\text{sc})}$, where $\mathcal{G}^{(0)}$ and $\mathcal{G}^{(\text{sc})}$ refer to the bulk and scattering parts of the Green tensor, respectively. Explicit expressions for the Green tensor in a cylindrical waveguide are compiled in Appendix A. This leads to the decomposition of the vdW potential into three terms [7, 16],

$$\begin{aligned} \mathcal{G}^2 &= \left(\mathcal{G}^{(0)} \right)^2 + \left(\mathcal{G}^{(\text{sc})} \right)^2 + 2\mathcal{G}^{(0)}\mathcal{G}^{(\text{sc})} \\ \Rightarrow U &= U^{(0)} + U^{(\text{sc})} + 2U^{(\text{cross})}. \end{aligned} \quad (4) \quad (5)$$

Each of these three terms has a clear physical meaning: the first ($U^{(0)}$) describes a loop of freely propagating photons that dominates in the near-field regime of distances $z \ll \lambda, R$, where it recovers the two-body potential in a homogeneous medium, i.e. the usual dipole-dipole near-field coupling with a r^{-6} distance scaling. The second

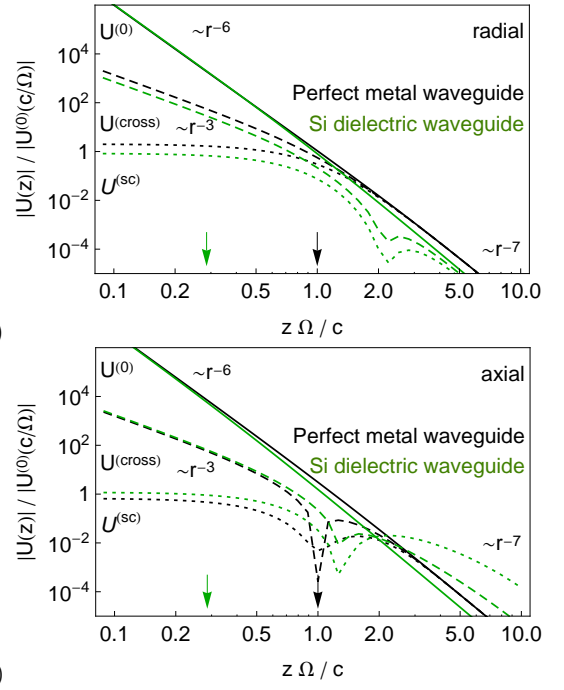


FIG. 2: Contributions to waveguide-mediated vdW coupling between two emitters inside a subwavelength hollow metallic cylinder (black curves) or dielectric cylinder waveguide (undoped silicon in vacuum, green curves) with radius $R = 0.8c/\Omega$. a) Radial dipole orientation and b) axial dipole orientation. The arrows indicate the onset of retardation at $z\sqrt{\epsilon_2}\Omega/c \approx 1$.

term ($U^{(\text{sc})}$) is due to loops formed by two scattered photons, and depends on the boundary conditions. At short distance, it approaches a constant value. The third term ($U^{(\text{cross})}$) consists of two-photon loops that involve only a single scattering event, and has a subleading r^{-3} scaling at short distance.

In the retarded regime $z \gg \lambda$, each of the three terms scales as r^{-7} . This is clearly seen in Fig. 2a) and b), where the three contributions are plotted for perfect metallic boundaries and for a dielectric waveguide. The two panels correspond to radial and axial dipole orientation, respectively. The material properties of the cylinder walls do not qualitatively change the scaling of the individual contributions to the dispersion force potential. In fact, a change in the boundary condition will mainly affect the peculiar properties of the discrete guided modes that can propagate in the waveguide. For all conductors, material properties have relatively little impact on the retarded potential which is dominated by the fluctuations of evanescent modes. We can expect that, in a scenario where one of the emitters is initially excited, the exchange of real photons may give rise to resonant contributions to the van der Waals interaction resulting in a much stronger dependence on the boundary conditions.

B. Perfectly reflecting cylinder

We first calculate the interaction potential in a perfectly reflecting waveguide using the scattering decomposition. In the far field ($z \gg \lambda, R$), the scattered Green tensor in an ideally reflecting waveguide exactly approaches the homogeneous one except for a sign change, which is mirrored in the contributions to the dispersion potential shown in Fig. 2a) and b) for radial and axial dipole orientation, respectively. We thus find from Eq. (1) that the cross-term nearly cancels the other two contributions, except for a small remainder with exponentially suppressed distance behavior, visible in Figs. 3 a) and b) that show the potential normalized to the value in free space for different cylinder radii. This surprisingly exact balance lies at the origin of the exponential behavior of the retarded potential, similarly encountered in the case of rectangular waveguides [11].

In order to see the exponential decay directly, it is helpful to use an alternative approach to the dyadic Green function that is better suited for perfectly conducting cylinders. As a consequence of Maxwell's equations, the tangential components of electric field have to vanish on the cylinder surface. Hence, the vector wave functions used in the expansion of the Green function are [18]

$$\mathbf{M}_{\sigma n \mu}^e(h) = \nabla \times \left[J_n(\mu r) \begin{matrix} \cos(n\varphi) e^{ihz} \\ \sin(n\varphi) e^{ihz} \end{matrix} \right], \quad (6)$$

$$\mathbf{N}_{\sigma n \lambda}^e(h) = \frac{1}{\sqrt{\lambda^2 + h^2}} \nabla \times \nabla \times \left[J_n(\lambda r) \begin{matrix} \cos(n\varphi) e^{ihz} \\ \sin(n\varphi) e^{ihz} \end{matrix} \right], \quad (7)$$

with $\mu = q_{nm}/R$ and $\lambda = p_{nm}/R$. Here, the numbers p_{nm} denote the m th root of the Bessel function of order n , $J_n(p_{nm}) = 0$, and q_{nm} the m th root of the derivative of the Bessel function of order n , $J'_n(q_{nm}) = 0$.

Expanding the Green function gives for $z \gtrsim z'$

$$\begin{aligned} \mathcal{G}(\mathbf{r}, \mathbf{r}', \omega) = & -\frac{\mathbf{e}_z \otimes \mathbf{e}_z}{k^2} \delta(\mathbf{r} - \mathbf{r}') \\ & + \sum_{n,m} \left[c_{\mu n} \mathbf{M}_{\sigma n \mu}^e(\pm k_\mu) \otimes \mathbf{M}_{\sigma n \mu}^e(\mp k_\mu) \right. \\ & \left. + c_{\lambda n} \mathbf{N}_{\sigma n \lambda}^e(\pm k_\lambda) \otimes \mathbf{N}_{\sigma n \lambda}^e(\mp k_\lambda) \right] \end{aligned} \quad (8)$$

with $k_\mu = \sqrt{k^2 - \mu^2}$, $k_\lambda = \sqrt{k^2 - \lambda^2}$, $k = \omega/c$, the normalization factors

$$c_{\mu n} = i \frac{(2 - \delta_{n0})}{4\pi\mu^2 I_{\mu n} k_\mu}, \quad c_{\lambda n} = i \frac{(2 - \delta_{n0})}{4\pi\lambda^2 I_{\lambda n} k_\lambda}, \quad (9)$$

and the overlap integrals

$$I_{\lambda n} = \int_0^R dr r J_n^2(\lambda r) = \frac{R^2}{2} J_n'^2(x), \quad x = p_{nm}, \quad (10)$$

$$I_{\mu n} = \int_0^R dr r J_n^2(\mu r) = \frac{R^2}{2} \left(1 - \frac{n^2}{q_{nm}^2} \right) J_n^2(q_{nm}). \quad (11)$$

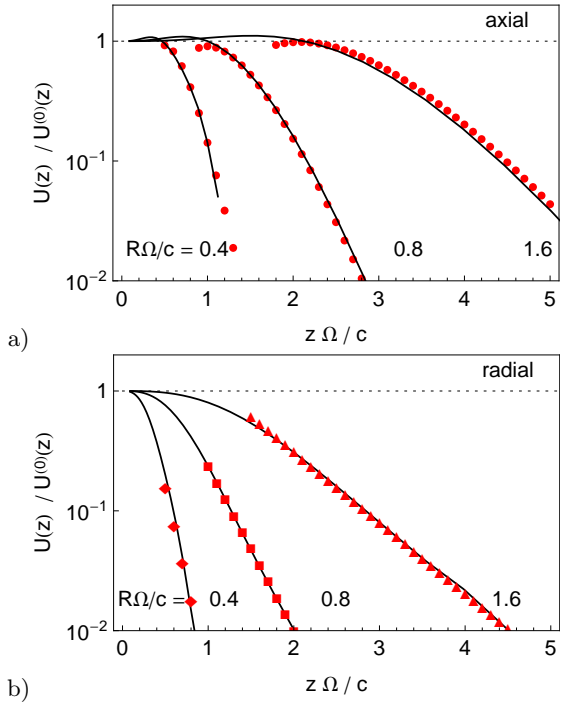


FIG. 3: Dispersion potential for two emitters in a perfectly reflecting hollow cylinder waveguide normalized to the free space potential (dotted line) with axial (a) and radial (b) polarizability for cylinder radii $R\Omega/c = 0.4, 0.8, 1.6$ (corresponding to 50nm, 100nm, 200nm at $\lambda = 780\text{nm}$). The dots indicate the asymptotic far field behavior of Eq. (18) to the axial component, and exponential fits to the radial component, respectively.

On the cylinder axis and setting $z > z' = 0$, only very few of the terms survive, and the result can be written as

$$\begin{aligned} \mathcal{G}(\mathbf{r}, \mathbf{r}', \omega) = & \frac{i}{4\pi} \sum_m \left[\left(\frac{e^{ik_\mu(z)}}{2I_{\mu 1} k_\mu} + \frac{k_\lambda e^{ik_\lambda z}}{2I_{\lambda 1} k^2} \right) \right. \\ & \left. \times (\mathbf{e}_r \otimes \mathbf{e}_r + \mathbf{e}_\varphi \otimes \mathbf{e}_\varphi) + \frac{\lambda^2 e^{ik_\lambda z}}{I_{\lambda 0} k_\lambda k^2} \mathbf{e}_z \otimes \mathbf{e}_z \right]. \end{aligned} \quad (12)$$

The van der Waals interaction between two dipoles in a perfectly reflecting cylinder possesses only two intrinsic length scales, the radius R of the tube and the dipole separation z . The limit $z/R \rightarrow 0$ corresponds to an increasingly large cylinder radius R or, alternatively, very close dipoles. In both cases, the van der Waals interaction in free space is recovered as follows. In the limit of large arguments, the Bessel functions become

$$J_n(x) \xrightarrow{x \gg 1} \sqrt{\frac{2}{\pi x}} \left[\cos \left(x - \frac{n\pi}{2} - \frac{\pi}{5} \right) + \mathcal{O} \left(\frac{1}{x} \right) \right] \quad (13)$$

and their zeros take the form $p_{nm} \simeq (m + \frac{n}{2} - \frac{1}{4})\pi$. Hence, the difference between adjacent zeros is $\Delta p_{nm} = p_{n,m+1} - p_{nm} \simeq \pi$ and thus $\Delta\lambda = \Delta p_{nm}/R \mapsto \pi/R$. In

this way, we find for example

$$\sum_m \frac{\lambda^2}{I_{\lambda 0} k_\lambda k^2} \xrightarrow{R \rightarrow \infty} \int_0^\infty d\lambda \frac{\lambda^3}{hk^2}, \quad (14)$$

which exactly reproduces the ($n = 0$)-contribution to the free-space Green function [19].

In the opposite limit, $z/R \rightarrow \infty$, the cylinder radius is small compared to the dipole separation. In this case, we can approximate the exponents as

$$k_\lambda z = \sqrt{(kR)^2 - p_{nm}^2} \left(\frac{z}{R} \right) \simeq i p_{nm} \left(\frac{z}{R} \right), \quad (15)$$

such that for an axial dipole the dominant contribution to the Green function reads

$$\mathcal{G}_{zz}(\mathbf{r}, \mathbf{r}', \omega) \simeq \frac{p_{01}}{2\pi k^2 R^3 J_1^2(p_{01})} e^{-p_{01}z/R} \mathbf{e}_z \otimes \mathbf{e}_z \quad (16)$$

where only the lowest (TM_{01}) mode with $p_{01} \simeq 2.405$ contributes. The van der Waals potential derived from this Green function is thus

$$U_{zz}(z) \simeq -\frac{\hbar\mu_0^2}{2\pi} \frac{p_{01}^2 c^4}{4\pi^2 J_1^4(p_{01}) R^6} e^{-2p_{01}z/R} \int_0^\infty d\xi \alpha_{zz}^2(i\xi) \quad (17)$$

which is seen to decay exponentially with increasing dipole separation. Compared to the van der Waals interaction in free space in the nonretarded limit, the exponential suppression is

$$\frac{U_{zz}(z)}{U_{zz}^{(0)}(z)} \simeq \frac{2p_{01}^2}{J_1^4(p_{01})} \left(\frac{z}{R} \right)^6 \exp \left[-2p_{01} \left(\frac{z}{R} \right) \right]. \quad (18)$$

Good agreement of the scaling is seen in Fig. 3a). The change of sign encountered in this component leads to an enhancement of the potential U_{zz} for axially polarized particles above the limit in a homogeneous medium at short distances. In contrast, the potential for radial polarization is always below the free-space value $U_{\perp}(z) \leq U_{\perp}^{(0)}(z)$. For this component the logarithmic plot suggests a different far-field scaling $U_{\perp}(z) \propto e^{-z} z^{-7}$ [fits in Fig. 3b)].

C. Conducting cylinder

We now assess numerically the impact of realistic materials. A concise representation of the Green function for a cylinder based on the scattering decomposition is given in App. A. The general boundary value problem is expressed in terms of reflection matrices that contain the dielectric functions, e.g. for a Drude metal and vacuum

$$\varepsilon_1(\omega) = 1 - \frac{\omega_p^2}{\omega(\omega + i\gamma)}, \quad \varepsilon_2 = 1. \quad (19)$$

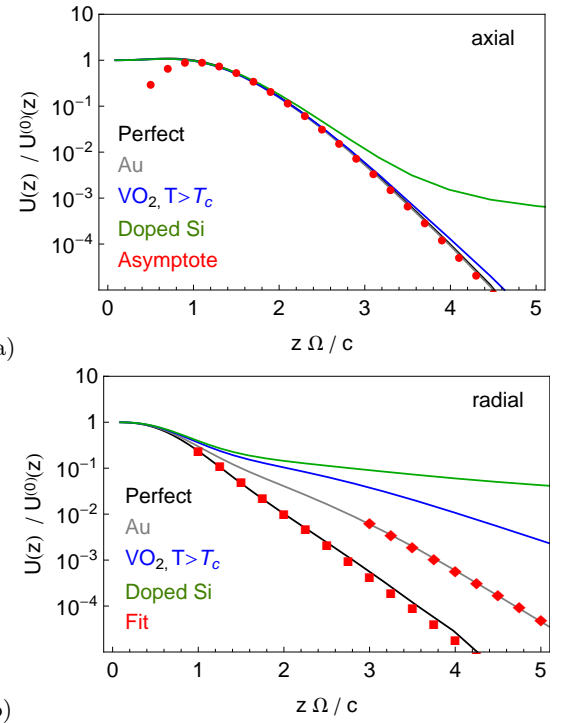


FIG. 4: Dispersion potential for two optical emitters in a hollow conducting cylinder ($\Omega = 2\pi c/780\text{nm}$, $Rc/\Omega = 0.8$) with axial (a) and radial (b) polarizability, normalized to the potential in free space. The curves correspond to a hollow waveguide with perfectly reflecting boundaries (black) or the material boundaries for gold (gray), VO_2 (blue), and doped silicon. The red dots indicate the asymptote [Eq. (18)] to the axial potential and suggest a weak dependence on material parameters. The red squares and diamonds are obtained from an exponential fit to the radial potential with a significant material dependence.

For gold, the relevant parameters are $\hbar\omega_p = 8.5\text{eV}$, $\gamma = 5 \times 10^{-3}\omega_p$ [20].

At optical wavelengths ($\lambda = 2\pi c/\Omega = 780\text{nm}$, $R = 0.8c/\Omega = 100\text{nm}$), we find that the impact of imperfect boundary conditions on the radially oriented dipoles is much stronger than on the axial one, see Fig. 4. Perfect boundaries and good conductors agree closely. The exponential fit to the potential for radially aligned dipoles agrees with an effective radius $R_{\text{eff}} = 130\text{nm}$, while the axial one is well-described with the asymptote of Eq. (18).

In order to understand the impact of a limited conductivity, we compare to the results obtained for hollow core fibers made out of weakly doped silicon (impurity concentration $1.3 \times 10^{18}\text{cm}^{-3}$) and metallic vanadium dioxide (VO_2 at $T > 340\text{K}$), which can be described by Lorentz-Drude models with the parameters given in Refs. [21, 22]. A numerical evaluation of the distance-dependent potentials (normalized to the bulk potentials) is shown in Fig. 4. As the conductivity is reduced, the boundaries become more penetrable, and the cancellation of scattered and free contributions is no longer exact. We see that the potential for axially polarized emit-

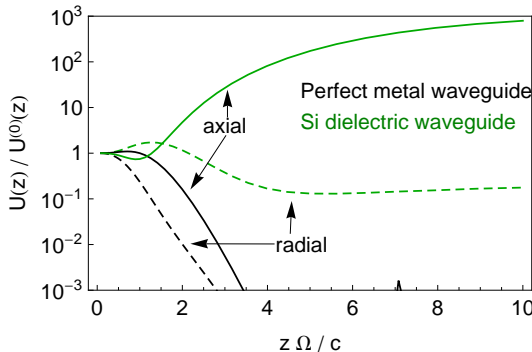


FIG. 5: Normalized dispersion potentials for two optical emitters inside a silicon cylinder in vacuum ($\Omega = 2\pi c/780\text{nm}$, $Rc/\Omega = 0.8$) with axial (solid green curve) and radial (dashed green curve) polarizability. The results for a perfectly conducting hollow tube (black curves) are given for comparison. The normalization refers to the bulk potential in the core medium.

ters inside a conducting VO_2 -capillary begins to deviate slightly from the perfect conductor limit, whereas for the doped silicon capillary, the far field potential recovers the z^{-7} -behavior. Again, the impact is much more drastic for the radial component.

An interesting question is whether the superconducting phase transition can lead to a significant modification of the dispersion potential. For an impure niobium sample the parameters in Eq. (19) should be chosen as $\hbar\omega_p = 10\text{eV}$, $\gamma = 6.5 \times 10^{-3}\omega_p$ [23]. A minimal – yet reasonable [24] – Meißner–London model for the superconducting state far from criticality is obtained by setting $\gamma \rightarrow 0$. Here, the Meißner length $\Lambda_L = c/\omega_p \approx 20\text{nm}$ describes the penetration of fields into the surface. At optical frequencies, the superconducting phase transition does not have a great effect, as the penetration into normally conducting niobium, described by the skin depth $\delta = \sqrt{2\gamma c^2/(\omega_p^2\omega)} \approx 5\text{nm}$, does not differ greatly from the Meißner–London length, so that both cases provide potentials similar to the one for gold in Fig. 4. For a lower transition frequency, e.g. for a Rydberg transition $|n, l = n - 1\rangle \rightarrow |n' = n + 1, l' = n\rangle$ with $n = 50$ at $\Omega = 2\pi \times 51\text{GHz}$ ($\lambda = 5.6\text{mm}$), we find that the normal skin depth $\delta \approx 500\text{nm}$ is much larger than the Meißner–London length. Hence, the superconductor can be expected to approximate even better an ideal reflector at GHz-frequencies. However, the variations are negligible with respect to the waveguide radius unless $R\Omega/c \ll 1$.

D. Solid dielectric cylinder

Similar to the transmission-line structures considered in Ref. [12], a dielectric waveguide features a fundamental mode without a frequency cut-off. Modifications of the results are expected due to the frequency-dependent mode profile in a dielectric waveguide. We assume solid

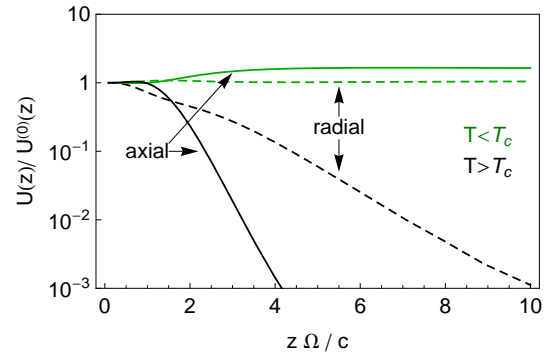


FIG. 6: Normalized dispersion potential for two emitters in a silicon cylinder embedded in VO_2 ($\Omega = 2\pi c/780\text{nm}$, $Rc/\Omega = 0.8$) with axial (solid curves) and radial (dashed curves) polarizability. At $T < T_c = 340\text{K}$, the cladding is dielectric and provides a weak dielectric waveguide (green curves) with moderate enhancement $U_{zz}(\infty)/U_{zz}^{(0)}(\infty) \approx 2$. Above the phase transition ($T > T_c$, black curves) the metallic cladding suppresses the far-field potential.

state emitters embedded in an undoped silicon cylinder suspended in vacuum, and impose a Drude–Lorentz model [22] that agrees well with the results of a simple index medium ($\epsilon_1 = 1$, $\epsilon_2 = 13.5$).

The resulting dispersion potentials in this structure for the two polarizations are compared in Fig. 5 to the potential in a perfectly conducting hollow cylinder. For the radial dipole orientation, we observe an enhancement by a factor of 2 at intermediate distances $zc/\Omega \approx 1$, similar to the effects found in the surface-assisted two-body potential [7]. This is connected with a change of sign in the cross term $U^{(\text{cross})}$, that indicates the change from a binding contribution at short distances to an antibinding contribution encountered at all distances for the conducting boundaries, see Fig. 2. For the axial dipole orientation, an enormous enhancement by three orders of magnitude with respect to the free space potential survives to large distances.

In both cases, the z^{-7} power laws are recovered in the far field, indicating that the subtle cancellation at work for the metallic waveguides is perturbed, especially for the axial dipole components. This can be clearly seen from the single contributions in Fig. 2. The scattered contribution $U^{(\text{sc})}$ can be identified as the origin of the significant enhancement in the potential of axially polarizable emitters.

E. Metal-insulator transition

The difference between a superconducting and a normal metal were found to be small, as both impose similar metallic boundary conditions. However, the drastic qualitative difference between the potentials encountered for dielectric waveguides and metallic ones, resulting from the existence of a fundamental mode or a mode

cut-off, respectively, suggest that materials with a metal-insulator transition may have a significant impact.

Vanadium dioxide (VO_2) is known to change from a dielectric to a metallic phase at $T_c = 340\text{K}$, and its impact on the Casimir interaction in coplanar cavities has been discussed before [22], based on Drude–Lorentz models of the dielectric function [21]. Interestingly, its refractive index in the dielectric state is slightly lower than that of undoped silicon, so that a silicon core embedded in VO_2 may be switched from a dielectric guide to a metallic one by a small increase in the temperature. This affects both polarization components as is clearly visible in the normalized potentials in Fig. 6. Due to the low index contrast, we obtain a leaky waveguide and at $T < T_c$ (green curves) the potential recovers closely the one in a homogenous medium. Still, the axial component is enhanced by roughly a factor of 2. As $T > T_c$ (black curves), the metallic boundary results in the exponential behavior already discussed in detail, so that the potential can be effectively switched off. Note that thermal corrections to the potential are negligible for optical transitions at the temperatures considered.

We expect an improved performance in a coated fiber in vacuum, where a VO_2 -layer in the insulating state would provide a situation close to a homogeneous dielectric cylinder with good waveguiding properties. This could recover the strong far-field enhancement encountered before. To generate a sufficiently strong boundary condition in the metallic state, the layer thickness should however exceed the skin depth ($\delta \approx 60\text{nm}$ at $\lambda = 780\text{nm}$).

III. OBSERVABLE FAR-FIELD POTENTIALS

If one of the emitters is not in its fundamental electronic state, the potential changes as a result of Förster-like processes [17, 25–28]

$$U_{ge}(z) = -U_{\text{vdW}}(z) + U_{\text{res}}(z). \quad (20)$$

The resonant potential arises from the exchange of real photons between the emitters via the guided mode. In metallic waveguides, this requires transition frequencies above the cut-off. In the single-mode regime, one can approximate the far field Green function by $\mathcal{G}(z, \omega) \approx i\beta \text{Im} [\mathcal{G}(0, \Omega)] \exp(i n_{\text{eff}} k |z|)$, where β describes the emitter-waveguide coupling efficiency and n_{eff} the mode index (see App. A 3). When bulk absorption is low, this results in interactions of infinite range, ultimately limited by the photon coherence $2z \approx c/\gamma$.

Unfortunately, the form of the resonant potential is still disputed in the literature [25, 26] and two forms are commonly obtained:

$$\begin{aligned} U_{\text{res}}^{\text{init}} &= |d^{(1)}|^2 \alpha^{(2)}(\Omega_1) \text{Re}([\mathcal{G}(\mathbf{r}_1, \mathbf{r}_2, \Omega_1)]^2) \\ &\propto \cos^2(n_{\text{eff}} k |z|), \end{aligned} \quad (21)$$

$$\begin{aligned} U_{\text{res}}^{\text{steady}} &= |d^{(1)}|^2 \alpha^{(2)}(\Omega_1) |\mathcal{G}(\mathbf{r}_1, \mathbf{r}_2, \Omega_1)|^2 \\ &\propto \text{const.} \end{aligned} \quad (22)$$

This seems to originate in different assumptions about the system dynamics. In fact, the first result is commonly encountered for a system initially prepared in a state $|e\rangle \otimes |g\rangle$ and left to free evolution, while the second arises from steady-state nonequilibrium configurations. Mathematically, the two forms result from different treatments of the double poles that arise in fourth-order perturbation theory. The first result is obtained by treating the poles as principal values, the second makes use of Sokhotsky's formula that also contains a δ -function contribution. On the basis of perturbation theory alone, the correctness of one or the other form of the resonant potential cannot be decided, as perturbation theory makes no statement as to how the poles should be circumvented. While the first case would yield an oscillating potential and force – as in free space –, the second potential is constant and, in consequence, force free. Arguments relating the resonant vdW potential between two dipoles to the dilute limit of the Casimir–Polder interaction between a dipole and a macroscopic body (known also nonperturbatively [29]) suggest that $U_{\text{res}}^{\text{init}}$ correctly describes systems left to free evolution [30]. A dynamical approach that involves solving the coupled atom-field dynamics within the framework of macroscopic QED supports this view [31].

More importantly, however, the nondecaying distance dependence may allow for the observation of the far-field dispersion potential between emitters, which has so far remained elusive due to the quickly decaying z^{-7} behavior in free space. At this point one might be tempted to try and use highly excited Rydberg atoms with their exaggerated vdW interaction to detect the retarded interaction. However, a straightforward inspection of the relevant scaling laws with the principal quantum number n [32] shows that this is not advantageous: the dipole moment matrix elements of neighboring dipole-coupled Rydberg states scale with $|d| \propto n^2$ and the associated transition frequencies as $\Omega \propto n^{-3}$. Hence, the polarizability is found to scale as $\alpha \propto n^7$. As the boundary between nonretarded and retarded regimes is set by the transition frequency as $z \simeq c/\Omega$, we immediately find that the vdW potential $U_{\text{vdW}}(z)$ at this distance is in fact suppressed by a factor $\propto n^{-7}$ compared to the ground-state potential. Similarly, resonant Förster processes that behave as $U_{\text{res}}(z) = C_3 z^{-3}$ with $C_3 \propto n^4$ are suppressed by a factor $\propto n^{-5}$. This is due to the fact that the benefit of a larger interaction strength is strongly outweighed by the rapid increase of the length scale at which the retarded regime sets in.

However, the resonant potential that requires propagating photons that are guided along the waveguide structure does not have the limitations as in free space. In this case one would expect to reach the retarded limit between two Rydberg atoms with an appreciable interaction strength.

IV. CONCLUSION

We have studied the vdW dispersion potential between two emitters placed inside a realistic metallic or dielectric waveguide with a subwavelength diameter. An exponentially decreased interaction potential was found for a perfectly reflecting boundaries, similar to the results for rectangular cross sections [11]. We found that the range of the potential can be modified by tuning the conductivity of the capillary wall. Fluctuations mediated by the fundamental mode in a dielectric waveguide, in contrast, can strongly enhance the far-field potential. This was previously unsettled due to the 3D nature of the guided modes [12]. The drastic qualitative difference between the potentials could allow to realize switchable dispersion potentials between solid-state emitters embedded in a dielectric waveguide core coated by a cladding featuring a metal-insulator phase transition. Finally, resonant contributions to the potential, arising from real-photon exchange via the guided mode, could bring the retarded dispersion interactions into the reach of experiments.

Acknowledgments

We gratefully acknowledge fruitful discussions with Francesco Intravaia, Simen Å. Ellingsen, Xuewen Chen, Ioannis Chremmos, Helge Dobbertin, and Vahid Sandoghdar. This work was partially supported by the DFG (grant no. SCHE 612/2-1).

Appendix A: Dyadic Green tensor in a cylinder

1. Bulk Green tensor

The Green tensor describes the field generated by an oscillating dipole source. In a bulk environment the field generated at a distance along the \hat{z} -axis can be expressed in the compact form [16],

$$\mathcal{G}_{\perp}^{(0)}(\mathbf{r}, \mathbf{r}', \omega) = -\frac{e^{ikz}}{4\pi k^2 z^3} (1 - ikz + k^2 z^2) \quad (\text{A1})$$

$$\mathcal{G}_{zz}^{(0)}(\mathbf{r}, \mathbf{r}', \omega) = \frac{e^{ikz}}{4\pi k^2 z^3} (2 - 2ikz). \quad (\text{A2})$$

Here, $k = \varepsilon\omega^2/c^2$ denotes the propagation constant in a medium with permittivity ε and $\mathcal{G}_{xx}^{(0)} = \mathcal{G}_{yy}^{(0)} = \mathcal{G}_{\perp}^{(0)}$. The form is useful for efficient numerical treatment. It can also be expressed in terms of cylindrical vector wave functions [33].

2. Scattered Green tensor

We consider a nonmagnetic dielectric cylinder of radius R (dielectric function ε_2), surrounded by another

homogeneous medium ε_1 , and decompose

$$\mathcal{G}(\mathbf{r}, \mathbf{r}', \omega) = \mathcal{G}^{(0)}(\mathbf{r}, \mathbf{r}', \omega) + \mathcal{G}^{(\text{sc})}(\mathbf{r}, \mathbf{r}', \omega) \quad (\text{A3})$$

into a free propagation part given by (A1) and a scattering term. We define the radial and total wave numbers in medium i , $\eta_i = k_i^2 - h^2$, $k_i^2 = \varepsilon_i(\omega)\omega^2/c^2$, and use a closed form given in Refs. [16, 33]

$$\begin{aligned} \mathcal{G}^{(\text{sc})}(\mathbf{r}, \mathbf{r}', \omega) = & \frac{i}{8\pi} \sum_{n=0}^{\infty} \int \frac{dh}{\eta_2^2} (2 - \delta_{n0}) \times \\ & \times \left[r_{MM} \mathbf{M}_{\sigma_n}^{e_n}(h, \eta_2) \otimes \mathbf{M}'_{\sigma_n}^{e_n}(-h, \eta_2) \right. \\ & + r_{NN} \mathbf{N}_{\sigma_n}^{e_n}(h, \eta_2) \otimes \mathbf{N}'_{\sigma_n}^{e_n}(-h, \eta_2) \\ & \pm r_{MN} \mathbf{M}_{\sigma_n}^{o_n}(h, \eta_2) \otimes \mathbf{N}'_{\sigma_n}^{o_n}(-h, \eta_2) \\ & \left. \pm r_{NM} \mathbf{N}_{\sigma_n}^{o_n}(h, \eta_2) \otimes \mathbf{M}'_{\sigma_n}^{o_n}(-h, \eta_2) \right]. \end{aligned} \quad (\text{A4})$$

Summation over upper and lower indices and global signs is assumed, e.g. $\pm \mathbf{A}_i \otimes \mathbf{B}'_l = +\mathbf{A}_i \otimes \mathbf{B}_j - \mathbf{A}_k \otimes \mathbf{B}_l$. The cylindrical vector wave functions are

$$\mathbf{M}_{\sigma_n}^{e_n}(h, \eta) = \nabla \times \left[J_n(\eta\rho) \frac{\cos(n\phi)}{\sin(n\phi)} \right] \hat{\mathbf{z}} e^{ihz} \quad (\text{A5})$$

$$\mathbf{N}_{\sigma_n}^{e_n}(h, \eta) = \frac{1}{k} \nabla \times \nabla \times \left[J_n(\eta\rho) \frac{\cos(n\phi)}{\sin(n\phi)} \right] \hat{\mathbf{z}} e^{ihz}, \quad (\text{A6})$$

where upper and lower cases refer to even and odd functions in ϕ . The function $J_n(x)$ denotes the Bessel function of the first kind, and a prime refers to the second spatial argument.

In the case of a single interface, we generalize the forms given in Ref. [34], to obtain the concise expressions

$$r_{\alpha}^{(n)} = -\frac{H_n^{(1)}(x)}{J_n(x)} \times \frac{A + B_{\alpha}}{A + C} \quad (\text{A7})$$

$$A = -n^2(R\omega/c)^2(hR)^2(\varepsilon_1 - \varepsilon_2)^2, \quad (\text{A8})$$

$$C = x_1^2 x_2^2 [\tilde{h}(x_1)x_2 - \tilde{j}(x_2)x_1][\varepsilon_1 \tilde{h}(x_1)x_2 - \varepsilon_2 \tilde{j}(x_2)x_1], \quad (\text{A9})$$

$$B_{MM} = x_1^2 x_2^2 [\tilde{h}(x_1)x_2 - \tilde{h}(x_2)x_1][\varepsilon_1 \tilde{h}(x_1)x_2 - \varepsilon_2 \tilde{j}(x_2)x_1], \quad (\text{A10})$$

$$B_{NN} = x_1^2 x_2^2 [\tilde{h}(x_1)x_2 - \tilde{j}(x_2)x_1][\varepsilon_1 \tilde{h}(x_1)x_2 - \varepsilon_2 \tilde{h}(x_2)x_1], \quad (\text{A11})$$

$$B_{MN} = -A + i n x_1^2 x_2 (Rk_2)(hR)(\varepsilon_2 - \varepsilon_1)[\tilde{h}(x_2) - \tilde{j}(x_2)], \quad (\text{A12})$$

where $x_i = R\sqrt{k_i^2 - h^2}$. We abbreviated $\tilde{h}(x) = \frac{d}{dx} \ln H_1^{(n)}(x)$, $\tilde{j}(x) = \frac{d}{dx} \ln J^{(n)}(x)$, where $H_1^{(n)}(x)$ denotes the Hankel function of the first kind. It may be useful to notice that the diagonal reflection matrices are even functions of h , while the off-diagonal ones are odd. By reciprocity, $r_{MN} = r_{NM}$, and causality requires that $\mathcal{G}(\mathbf{r}, \mathbf{r}', -\omega^*) = \mathcal{G}^*(\mathbf{r}, \mathbf{r}', \omega)$.

For ideally reflecting surfaces ($\varepsilon_1 \rightarrow -\infty$) the reflection matrices take the simple form [34]

$$r_{MM}^{(n)} = -\frac{H_n^{(1)}(x)}{J_n(x)}, \quad r_{NN}^{(n)} = -\frac{H_n^{(1)}(x)}{J_n(x)} \frac{\tilde{h}(x)}{\tilde{j}(x)}, \quad (\text{A13})$$

$$r_{MN}^{(n)} = r_{NM}^{(n)} = 0. \quad (\text{A14})$$

On the cylinder axis ($\rho, \rho' \rightarrow 0$) only the lowest multipole waves with $n = 0, 1$ contribute. We choose $\phi = \phi' = 0$ and $z' = 0$ for simplicity, so that the Green tensor depends only on the axial displacement z . This gives

$$\mathcal{G}_{zz}^{(\text{sc})}(z, \omega) = \frac{i}{8} \int \frac{dh}{2\pi} e^{ihz} \left[2 \frac{\eta_2^2}{k_2^2} r_{NN}^{(0)} \right] \quad (\text{A15})$$

$$\mathcal{G}_{\perp}^{(\text{sc})}(z, \omega) = \frac{i}{8} \int \frac{dh}{2\pi} e^{ihz} \left[r_{MM}^{(1)} - \frac{2ih}{k_2} r_{MN}^{(1)} + \frac{h^2}{k_2^2} r_{NN}^{(1)} \right]. \quad (\text{A16})$$

The integral can be immediately performed at imaginary frequencies. At real frequencies, parity arguments allow to map the integrand to $\omega \in [0, \infty]$. A numerical integration can be performed along a path in the complex h -plane that avoids the region $h \in [\sqrt{\varepsilon_2} \omega/c, \sqrt{\varepsilon_1} \omega/c]$

from below and is slightly shifted into the upper plane elsewhere for improved convergence.

3. Guided mode contributions

The fundamental guided mode corresponds to the pole of the reflection matrices at a value $\tilde{h} = n_{\text{eff}}\omega/c$, which can easily be found numerically. The residue theorem is applied to evaluate the pole contribution. This corresponds to replacing $\frac{A+B_\alpha}{A+C} \rightarrow i\pi\delta(h - \tilde{h}) \frac{A+B_\alpha}{\partial(A+C)/\partial h}$ in Eqs. (A15) and (A16). The pole contribution provides dominates the far field, so that

$$\mathcal{G}(z, \omega) \approx i\beta \text{Im} [\mathcal{G}(0, \omega)] \exp(in_{\text{eff}}|z|\omega/c) \quad (\text{A17})$$

and has a harmonic spatial dependence [35]. In lossy environments, where the poles are removed from the real axis, their contribution can be found by a numerical contour integration or a Lorentzian fit to the integrand [36]. Note that the group velocity of homogeneous propagation due to $\mathcal{G}^{(0)}$ differs from the one of the guided mode and may result in a small beating of the amplitude at short and intermediate distances.

[1] F. London, Z. Phys. A **63**, 245 (1930).

[2] H. B. Casimir and D. Polder, Phys. Rev. **73**, 360 (1948).

[3] A. Salam, *Molecular Quantum Electrodynamics: Long-Range Intermolecular Interactions* (Wiley, Hoboken, 2010).

[4] S. Y. Buhmann, *Dispersion forces I — Macroscopic Quantum Electrodynamics and Ground-State Casimir, Casimir-Polder and van der Waals Forces* (Springer, Berlin, 2012).

[5] J. Mahanty and B. Ninham, *Dispersion forces*, vol. 5 (Academic Press, London, 1976).

[6] S. Spagnolo, R. Passante, and L. Rizzato, Phys. Rev. A **73**, 062117 (2006).

[7] H. Safari, S. Y. Buhmann, D. Welsch, and T. D. Ho, Phys. Rev. A **74**, 042101 (2006).

[8] R. Passante and S. Spagnolo, Phys. Rev. A **76**, 042112 (2007).

[9] S. Y. Buhmann, H. Safari, S. Scheel, and A. Salam, Phys. Rev. A **87**, 012507 (2013).

[10] S. Å. Ellingsen, S. Y. Buhmann, and S. Scheel, Phys. Rev. A **82**, 032516 (2010).

[11] E. Shahmoon and G. Kurizki, Phys. Rev. A **87**, 062105 (2013).

[12] E. Shahmoon, I. Mazets, and G. Kurizki, Proc. Natl. Acad. Sci. **111**, 10485 (2014).

[13] T. G. Walker and M. Saffman, Phys. Rev. A **77**, 032723 (2008).

[14] D. Cano and J. Fortágh, Phys. Rev. A **86**, 043422 (2012).

[15] L. Knöll, S. Scheel, and D. Welsch, in *Coherence and Statistics of Photons and Atoms*, edited by J. Perina (Wiley, New York, 2001), arXiv: quant-ph/0006121.

[16] S. Scheel and S. Buhmann, Acta Phys. Slov. **58**, 675 (2008).

[17] H. R. Haakh, J. Schiefele, and C. Henkel, Int. J. Mod. Phys. Conf. Series **14**, 347 (2012), arXiv: 1111.3748.

[18] C.-T. Tai, *Dyadic Green functions in electromagnetic theory* (IEEE Press, 1994).

[19] L.-W. Li, P.-S. Kooi, M.-S. Leong, and T.-S. Yeo, J. Electromag. Waves Appl. **8**, 663 (1994).

[20] E. Palik, *Handbook of Optical Constants of Solids II* (Academic Press, San Diego, 1991).

[21] H. W. Verleur, A. Barker Jr, and C. Berglund, Phys. Rev. **172**, 788 (1968).

[22] I. Pirozhenko and A. Lambrecht, Phys. Rev. A **77**, 013811 (2008).

[23] S. Perkowitz, G. L. Carr, B. Subramaniam, and B. Mitrović, Phys. Rev. B **32**, 153 (1985).

[24] G. Bimonte, H. Haakh, C. Henkel, and F. Intravaia, J. Phys. A **43**, 145304 (2010).

[25] L. Gomberoff, R. R. McLone, and E. A. Power, J. Chem. Phys. **44**, 4148 (1966).

[26] E. A. Power and T. Thirunamachandran, Phys. Rev. A **51**, 3660 (1995).

[27] A. E. Cohen and S. Mukamel, Phys. Rev. Lett. **91**, 233202 (2003).

[28] Y. Sherkunov, Phys. Rev. A **79**, 032101 (2009).

[29] S. Y. Buhmann and S. Scheel, Phys. Rev. Lett. **100**, 253201 (2008).

[30] H. Safari and M. R. Karimpour, Phys. Rev. Lett. **114**, 013201 (2015).

[31] P. Barcellona, R. Passante, L. Rizzato, and S. Y. Buhmann (2015), arXiv: 1503.0098.

[32] T. F. Gallagher, *Rydberg atoms* (Cambridge University Press, Cambridge, 1994).

- [33] L. Li, M. Leong, T. Yeo, and P. Kooi, *J. Electromag. Waves Appl.* **14**, 961 (2000).
- [34] S. Å. Ellingsen, S. Y. Buhmann, and S. Scheel, *Phys. Rev. Lett.* **104**, 223003 (2010).
- [35] A. González-Tudela, D. Martin-Cano, E. Moreno, L. Martin-Moreno, C. Tejedor, and F. J. Garcia-Vidal, *Phys. Rev. Lett.* **106**, 020501 (2011).
- [36] D. Dzsotjan, A. S. Sørensen, and M. Fleischhauer, *Phys. Rev. B* **82**, 075427 (2010).